Mat. Res. Soc. Symp. Proc. Vol. 746 © 2003 Materials Research Society Q1.4

Single Crystal High Frequency Cavity-based EPR Spectroscopy of Single Molecule Magnets

S. Hill,[1] R. S. Edwards,[1] S. I. Jones,[1] S. Maccagnano,[1] J. M. North,[2] N. Aliaga,[3] E-C. Yang,[4] N. S. Dalal,[2] G. Christou,[3] D. N. Hendrickson[4]
[1]Department of Physics, University of Florida, Gainesville, FL 32611-8440, USA
[2]Department of Chemistry, Florida State University, Tallahassee, FL 32310, USA
[3]Department of Chemistry, University of Florida, Gainesville, FL 32611-8440, USA
[4]Department of Chemistry and Biochemistry, University of California at San Diego, La Jolla, CA 92093, USA

ABSTRACT

We report high frequency electron paramagnetic resonance (EPR) investigations of a series of high spin (total spin up to S = 10) manganese and nickel complexes which have been shown to exhibit single molecule magnetism, including low temperature (below ~ 1K) hysteresis loops and resonant magnetic quantum tunneling. A cavity perturbation technique enables high sensitivity oriented single crystal EPR measurements spanning a very wide frequency range (16 to 200+ GHz). Fitting of the frequency and field orientation dependence of EPR spectra allows direct determination of the effective spin Hamiltonian parameters. Studies on a range of materials with varying (approximately axial) site symmetries facilitates an assessment of the role of transverse anisotropy (terms in the Hamiltonian that do not commute with $\hat{S}_z$) in the magnetic quantum tunneling phenomenon.

INTRODUCTION

Single molecule magnets (SMMs) have stimulated considerable experimental and theoretical research interest since the discovery of resonant quantum tunneling of the magnetization (QTM) in Mn_{12}-acetate in 1996 [1]. Their main attraction is an intrinsic bistability which is realized via a large spin ground state (up to $26\mu_B$) and a significant axial (easy-axis) magnetocrystalline anisotropy [2,3]. This bistability has aroused great interest in terms of the use of SMMs in future molecular devices [4]. When grown as single crystals, the SMM unit is monodisperse—each molecule in the crystal has the same spin, orientation, magnetic anisotropy and structure. Thus, SMMs enable fundamental studies of properties intrinsic to magnetic nanostructures that have previously been inaccessible.

All of the SMMs of interest possess a dominant uniaxial magnetocrystalline anisotropy and, to lowest order, the effective spin Hamiltonian may be written

$$\hat{H} = D\hat{S}_z^2 + \mu_B \vec{B} \cdot \overleftrightarrow{g} \cdot \hat{S} + \hat{H}', \qquad (1)$$

where D (< 0) is the uniaxial anisotropy constant, the second term represents the Zeeman interaction with an applied field B, and $\hat{H}'$ includes higher order terms in the crystal field, as well as environmental couplings such as intermolecular dipolar and exchange interactions [1-7]. This Ising-type anisotropy is responsible for the energy barrier to magnetization reversal and the resulting magnetic bistability – factors which lead to magnetic hysteresis at sufficiently low temperatures [1-3]. Unlike bulk magnets, this hysteresis is intrinsic to each individual molecule – hence the term SMM. However, essentially all SMMs continue to exhibit slow magnetic

relaxation, even as T → 0 K. This low temperature relaxation is due to quantum tunneling, whereby non-axially symmetric interactions in $\hat{H}'$ cause the mixing of states of opposite magnetic polarity necessary for tunneling to occur [2,3].

One of the major goals in the design of future SMMs is to be able to control QTM so that it may be exploited for possible applications. For example, tunneling should be suppressed if one is to use SMMs for data storage applications, whereas an ability to switch coherent tunneling on and off could prove useful for quantum computation [4]. Tunnel rates depend on the degree of symmetry breaking ($\hat{H}'$), which is something which can be determined very precisely via single crystal EPR measurements [5-9]. However, the $(2S + 1)$-fold quantum energy level structure associated with a large molecular spin S necessitates spectroscopies spanning a wide frequency range. Furthermore, large zero-field level splittings, due to the significant magnetocrystalline anisotropy (large $|D|$) and large total spin S, demand the use of frequencies and magnetic fields considerably higher (50 GHz to 1 THz, and up to 10+ tesla respectively) than those typically used by the majority of EPR spectroscopists. An important breakthrough, therefore, in the spectroscopy of SMMs has been the development of sensitive cavity perturbation techniques for carrying out multi-high-frequency (20 to 200+ GHz) EPR measurements on single crystals [5-10]. In particular, this technique leads to at least a three orders of magnitude improvement in detection sensitivity relative to conventional single-pass multi-high-frequency EPR techniques, which opens up many important new avenues for probing SMMs. Furthermore, as we shall demonstrate in this article, studies on oriented single crystals enable precise characterizations of weak interactions in $\hat{H}'$ which turn out to be crucial as far as QTM is concerned.

The article is organized as follows: in the next section, we describe our experimental setup and procedures in detail, with emphasis on high-frequency EPR applications; this account of our technique expands upon an earlier article [10] which deals with the construction and characterization of cavity based microwave instrumentation for probing the electrodynamic response of conducting samples. We then provide a series of brief examples of the unique capabilities of this instrumentation, with emphasis on multi-frequency oriented single crystal measurements. This is followed by a short summary.

EXPERIMENTAL

Documented lack of resolution, sensitivity and/or various experimental artifacts have been known to affect most high frequency EPR investigations of SMMs to date. First of all, the low sensitivity usually limits possible studies to powder samples or aligned polycrystals, since single crystals are typically too small to detect a useful EPR signal. Even in the case of large polycrystalline samples, often only a few transitions are observed [11,12]. Furthermore, misalignment of polycrystals, stresses in pressed powders, or uncontrolled field-alignment of micro-crystallites in loose powders are all factors which may introduce unwanted experimental artifacts, particularly as far as EPR lineshape analyses are concerned. In addition, it is commonly stated that observed EPR lineshapes cannot be analyzed because they contain uncontrollable distortions caused by standing waves in the sample probe, which result in a mixing of the dissipative and reactive sample response [13,14,15]. As an example, it has been reported in [14] that the linewidths in Fe_8Br approximately scale as M_S^2 (where M_S is the spin projection of the state from which the transition is excited), whereas our earlier studies [5-9] have shown a dominant linear dependence of the linewidths on M_S, both for Fe_8Br and Mn_{12}-acetate.

As we will show in the following results section, measurements on single crystals are essential for studies of SMMs, as are several other unique aspects of our technique. For example, contrary to recent assertions [15], we *are* able to obviate essentially all instrumental artifacts that could influence/distort EPR line shapes. In addition, our ability to measure at many frequencies, temperatures and field orientations enables us to distinguish between many contributions to the EPR line widths and shapes. These include: inter-SMM and hyperfine dipolar fields; distributions in crystal field parameters; and spin-lattice interactions. Indeed, each of these effects have been discussed extensively in the QTM literature, *e.g.* dipolar fields [16], distributed crystal field parameters caused by dislocations [17,18] or solvent and ligand disorder [19], and hyperfine interactions [20].

The high degree of sensitivity required for single crystal measurements is achieved using a resonant cavity perturbation technique in combination with a broad-band Millimeter-wave Vector Network Analyzer (MVNA) exhibiting an exceptionally good signal-to-noise ratio; a detailed description of this instrumentation can be found in ref. [10]. The MVNA is a phase sensitive, fully sweepable (8 to 500+ GHz [10]), superheterodyne source/detection system. Several sample probes couple the network analyzer to a range of high sensitivity cavities (Q–factors of up to 25,000) situated within the bore of a 7 tesla superconducting magnet. The MVNA/cavity combination has been shown to exhibit a sensitivity of at least 10^9 spins.$G^{-1}.s^{-1}$, which is comparable with the best narrow-band EPR spectrometers. This, coupled with newly acquired sources and a split-pair magnet, enables single crystal measurements at any frequency in the range from 8 to 500 GHz, at temperatures down to 1.5 K (±0.01 K), and for any geometrical combination of DC and AC field orientations up to 7 T (up to 45 T at the National High Magnetic Field Laboratory).

The use of a narrow band cavity offers many important advantages over non-resonant methods (see *e.g.* refs [5,8-10]). Careful consideration concerning the coupling of radiation to and from the cavity (via waveguide), combined with the ability to study very small samples, eliminates problems associated with standing waves in the sample probe [10]. This, in turn, eliminates a mixing of the dissipative and reactive responses of the sample under investigation and, when combined with a vector detection scheme, enables faithful extraction of the true EPR lineshapes (both the real and imaginary components), free from instrumental artifacts. One other notable feature of the superheterodyne scheme is its detection rate of 34 MHz; thus, there is no need for field modulation, unlike other high field EPR methods [13]. Consequently, the raw data displayed in this paper constitute pure absorption. Finally, the use of a cavity enables positioning of a single crystal sample into a well defined electromagnetic field environment, *i.e.* the orientations of the DC and AC magnetic fields relative to the sample's crystallographic axes are precisely known, and the DC field is very homogeneous over the tiny volume (< 1 mm^3) of the sample. In this way, additional contributions to the EPR lineshapes are avoided due to, *e.g.* field inhomgeneities over the sample volume, or slight mis-alignments of crystallites, as may be the case for measurements on aligned powders.

In order to facilitate coupling between the spectrometer (MVNA) and the cavity, we have constructed various waveguide probes, optimized to work in various frequency bands up to about 200 GHz. Each probe consists of two waveguides for separately coupling the source and detector to the cavities. Composite waveguide materials (copper and gold plated stainless steel) are used both to minimize microwave losses and to maximize thermal isolation of the cold part of the probe. Rectangular and cylindrical cavities may be readily interchanged (at room temperature), as can the coupling to the cavity. A detailed description of the construction of these probes (with

detailed schematics), as well as extensive technical parameters associated with the cavities, are presented elsewhere [10]. Although the best results are usually achieved at the fundamental mode of a particular cavity (together with the appropriate coupling), exceptional results may also be achieved in over-moded cavities. In particular, high Q-factor cylindrical cavities permit measurements up to frequencies several times the fundamental mode frequency. Thus, broad band spectroscopy is possible, whilst maintaining many of the advantages of a narrow band cavity. The high Q-values (up to 10^4 at frequencies as high as 200 GHz) ensure well separated cavity modes which we can characterize with the MVNA prior to making a measurement; this procedure is described in more detail in ref. [10]. Furthermore, careful positioning of a tiny single crystal on the side walls of the cavity ensures that the sample sits in a magnetic field antinode for any mode of the cavity, as required for EPR. While these procedures have been extensively tested to frequencies on the order of 200 GHz, we have recently succeeded in extending measurements up to 300 GHz using low frequency (< 200 GHz) probes. However, for measurements above 200 GHz, a quasi-optical system is under construction which will be described in a future publication.

In order to enable in-situ rotation of the sample relative to the applied magnetic field, we utilize a split-pair magnet with a 7 T horizontal field and a vertical access. Smooth rotation of the entire rigid microwave probe, relative to the fixed field, is achieved via a room temperature stepper motor mounted at the neck of the magnet dewar; the stepper motor offers 0.01° angle resolution. The source and detector are bolted rigidly to the microwave probe; subsequent connection to and from the MVNA is achieved via flexible coaxial cables [10]. In this mode of operation, one can maintain optimal coupling between the spectrometer and the cavity containing the sample, *whilst* rotating the probe. As discussed in great detail in ref. [10], good coupling between the various microwave elements is essential in order to maintain a high sensitivity and a low noise level. Rotation of the entire rigid sample probe also ensures that the sample sits in a reproducible electromagnetic field environment for all measurements made on a particular mode of the cavity.

Temperature stabilization is achieved using a fully automated Quantum Design PPMS variable helium flow system; the control software for the PPMS also automates field sweeps and rotation of the sample probe. All of the data presented in this article were obtained by sweeping the magnetic field at a constant frequency, temperature and field orientation; however, it is also possible to sweep the temperature and field orientation. Fixed frequency measurements are then repeated at many different temperatures, frequencies and field orientations.

In the next section, we present data for the following SMM samples: $[Mn_{12}O_{12}(CH_3COO)_{16}(H_2O)_4]\cdot 2CH_3COOH\cdot 4H_2O$ (Mn_{12}-acetate), $[Mn_4O_3Cl_4(O_2CEt)_3py_3]_2$, and $[Ni(hmp)(R\text{-}OH)Cl]_4$ (R = Me, Et and tBuEt). Details concerning the preparation of these materials are presented elsewhere [21-23]. The typical sizes of single crystals range from $1.4 \times 0.16 \times 0.16$ mm^3 to $1.5 \times 1.5 \times 2.5$ mm^3, and the shapes range from needles to flat platelets to distorted cubes. For many of the higher symmetry SMMs, fairly accurate alignment of the crystals can be achieved when mounting the samples in the cavity prior to cooling. For lower symmetry SMMs, in-situ rotation about several axes is usually required in order to locate the principle magnetic axes of the samples. Particular care is taken to avoid solvent loss, since this can affect both the quality of the data and, in some cases, this may even affect the underlying physics of the SMMs. The samples are removed from their mother liquor and transferred to the cavity in a matter of a few minutes; in some extreme cases, the samples are coated in a protective layer of grease immediately upon removing them from the mother liquor. The samples are then

cooled at about 10 K/min, initially under 1 atmosphere of helium gas; the pressure is only reduced at low temperatures. Silicone grease is used to secure samples within the cavity.

RESULTS

In this section, we give an overview of some of the recent data that have been obtained for several SMMs using the instrumentation described above. The first example involves the Mn_{12}-acetate spin $S = 10$ system, which was the first SMM and remains the most widely studied. The Mn_{12} molecule has a high S_4 symmetry and, therefore, exhibits very slow quantum relaxation at low temperatures. There has been a considerable effort to determine the symmetry breaking which is responsible for this tunneling. Recent studies clearly show that for a typical crystal, there is a distribution of tunnel splittings, *i.e.* there is a molecule-to-molecule variation in the magnitude of the transverse interactions responsible for the tunneling. It has long been assumed that the rhombic crystal field term ($\hat{O}_4^2$) in $\hat{H}'$ (Eq. 1) is zero for Mn_{12}-acetate due to its S_4 site symmetry; for this reason, other sources of symmetry breaking are required in order to explain the QTM. While high-frequency EPR [13] and neutron studies [24] have provided convincing evidence for a fourth order single-ion transverse anisotropy ($\hat{O}_4^4$), such an interaction cannot explain many key experimental factors associated with the observed low-temperature hysteresis [25]. For this reason, recent theoretical and experimental efforts have focused on the possible role played by disorder [17-19,26].

Cornia *et al.* have proposed a model in which disorder in the solvent molecules surrounding the Mn_{12} molecule gives rise to a local transverse quadratic anisotropy [19], *i.e.* a local rhombic distortion. Such a disorder may be expected to result in several distinct species (isomers) of Mn_{12}-acetate, each having slightly different (*i.e.* a distribution) tunnel splittings caused by the slightly different solvent-disorder-induced rhombic terms in $\hat{H}'$. Such a model is quite appealing, since magnetic relaxation experiments clearly indicate a distribution in the tunnel splittings for Mn_{12}-acetate [26]. An alternative model proposed by Garanin and Chudnovsky involves a transverse quadratic anisotropy induced via dislocations [17,18]. The long range strains produced by these dislocations are predicted to result in very broad distributions of the tunnel splittings, indeed, probably much broader distributions than are observed experimentally [26]. While both disorder pictures can explain many aspects of the reported magnetic relaxation experiments, their respective spectroscopic signatures may be expected to be quite different.

Before presenting direct spectroscopic evidence for both quartic and quadratic transverse interactions in Mn_{12}-acetate, we should point out that our earlier investigations highlighted the significant effect that disorder has on EPR spectra obtained for fields parallel to the magnetic easy axis of the Mn_{12} molecule [5-9]. For this geometry, the spectra are most sensitive to diagonal terms in Eq. 1, *i.e.* $D\hat{S}_z^2$ and higher order terms such as $B_4^0\hat{O}_4^0$; these studies confirmed the existence of a significant D-strain (σ_D up to 2%) in Mn_{12}-acetate single crystals [5-9]. While these results hinted at the importance of disorder in the tunneling mechanism, they did not identify the transverse terms in Eq. 1 responsible for the tunneling. To do so, one has to measure spectra with the applied field transverse to the magnetic easy axis of the molecule. For this geometry, the EPR spectra exhibit maximum sensitivity to the transverse terms in $\hat{H}'$ (Eq. 1). Indeed, spectra obtained as a function of angle within the hard plane of the molecule may be used to deconvolute several different contributions to the transverse anisotropy, as demonstrated by means of Figure 1.

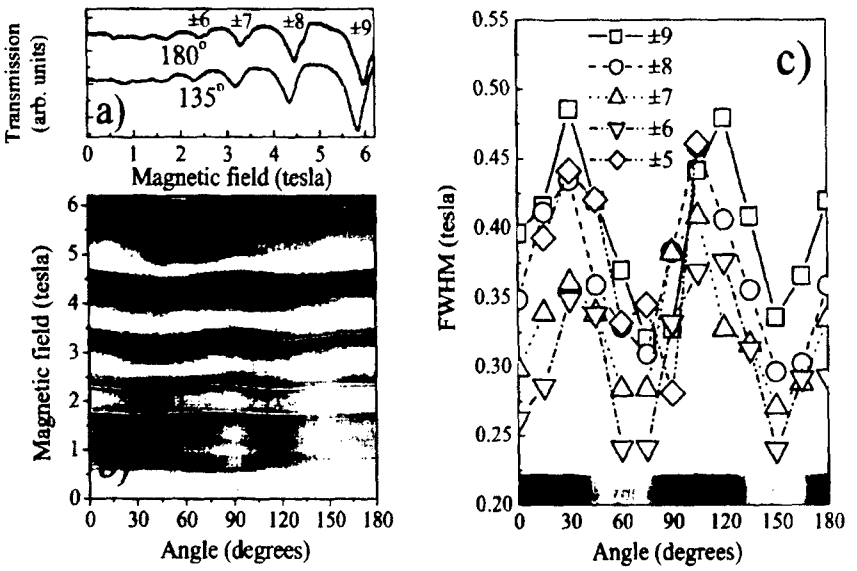

Figure 1. a) Two typical hard plane transmission spectra obtained for Mn_{12}-acetate (the in-plane field orientations are given in the figure); the frequency is 49.86 GHz, and the temperature is 15 K. The dips in transmission correspond to EPR absorptions between pairs of levels that evolve from the $\pm M_S$ levels (see labels) in zero field [8]. b) Contour plot of the angle dependence of the EPR absorption intensity (dark) for field rotations in the hard plane. The white lines are fits to the peak positions. c) Angle dependence of the EPR linewidths (FWHM) for the various transitions in a); see text for explanation of shaded region in the lower part of the figure.

The contour plot in Figure 1b demonstrates a pronounced four-fold pattern in the central positions (in field) of the EPR absorptions as a function of the orientation of the magnetic field within the hard plane of the molecule. This four-fold pattern is intrinsic to the Mn_{12} molecule, and can be attributed to a quartic transverse zero-field interaction of the form $(\hat{S}_+^4 + \hat{S}_-^4)$ in $\hat{H}$'. Fits to the angle dependence (solid white curves) are consistent with a single value of the coefficient $B_4^4 = 3.2(1)\times10^{-5}\,\mathrm{cm}^{-1}$. These fits also include a small two-fold correction, which is due to unavoidable misalignments of the sample's (~1°) easy axis with the field rotation axis; this effect *is not* related to any transverse zero-field interaction. Figure 1a shows raw transmission spectra obtained for two different orientations of the magnetic field within the hard plane. The $\psi = 135°$ is extremely simple, showing nice symmetric EPR absorptions. On the other hand, the $\psi = 180°$ spectrum exhibits a high field shoulder on each of the peaks. This splitting of the peaks for the hard plane spectra has been seen in several samples [8], and also by other groups [19]. Indeed, Cornia *et al.* have proposed that its origin is connected with the solvent disorder which leads to a local lowering of the symmetries of the Mn_{12} molecules [19].

It is no coincidence that the angle separation is 45° between the clean trace and the trace exhibiting the shoulder in Figure 1a. This again signifies an effect with a four-fold symmetry, however, its origin is related to a disorder-induced two-fold rhombic distortion, as will be

explained below. The split double peaks ($\psi = 180^{\circ}$) are very similar to those observed by Cornia *et al.* [19], and their spacing of about 0.35 T also agrees. To emphasize the correlation between the shoulder and disorder, we plot the full width at half maximum (FWHM) of several of the peaks, as a function of ψ, in Figure 1c; ψ is merely a measure of the field orientation relative to a fixed arbitrary direction within the hard plane of the sample. The shaded strip at the bottom of Figure 1c signifies the strength of the observed shoulder seen in Figure 1a (darker implies stronger); the shoulder is most pronounced at angles slightly below the maxima in the linewidths.

Assuming that the fine structure (shoulder) and line broadening are due to local rhombic distortions, then the angle dependence has a natural explanation. The quadratic term in $\hat{H}'$ has the form $E(\hat{S}_x^2 - \hat{S}_y^2)$, which produces a two-fold pattern for rotations in the hard plane. An intrinsic quadratic anisotropy of this form would produce shifts in the hard axis EPR peak positions, contrary to what is observed. However, in the case of Cornia's model (involving ligand disorder [19]) one expects equal numbers of molecules having positive and negative E. This is because the disorder involves an acetate ligand which can take four different positions (90° apart) about the z-axis of the molecule; a change in the sign of E merely corresponds to a 90° rotation of the hard axis. Thus, one expects overlapping two-fold patterns with a 90° phase shift, corresponding to molecules with their disorder-induced hard axes oriented at 90° to each other. The 90° phase shift results in line broadening rather than line shifts. What is more, the effect on the linewidths will exhibit a four-fold pattern, as opposed to a two-fold one, *i.e.* the S_4 symmetry is only broken locally, whereas EPR measures a global average of this disorder. Based on these studies, we estimate an E term associated with the disorder of about 0.01 cm^{-1}.

Studies for some other samples show additional fine structures. We believe this to be a consequence of a higher resolution in intrinsically cleaner samples, *i.e.* samples having intrinsically narrower EPR lines. such multiple fine structures may signify additional configurations of the acetate ligands, all possible combinations of which have been discussed in ref. [19]. Indeed, it is likely that different ligand disorders will have different associated hard directions, and this might explain why the shoulders seen in Figure 1 are observed slightly away from the maxima in the linewidths. We note also, that there is an approximately 10° shift in the four-fold patterns observed in Figure 1b due to the intrinsic four-fold transverse interaction, and the disorder induced patterns seen in Figure 1c. Finally, temperature dependent measurements (not shown) provide the final confirmation that the splitting is due to distinct ground states, presumably different ligand isomers. Both components of the splitting persist to the lowest temperatures investigated, while the intensity in all of the excited state transitions vanishes as $T \rightarrow 0$, *i.e.* the shoulder in Figure 1a corresponds to a distinct ground state.

Next we turn to a manganese system in which the magnetic unit consists of a dimer of Mn_4 cubes, with the formula $[Mn_4O_3Cl_4(O_2CEt)_3py_3]_2$ (denoted NA3 for short) [22]. Hysteresis experiments for this complex also show resonant QTM steps [27]. However, no tunneling is seen in zero-field – a behavior which is quite different from that observed for essentially all known monomeric SMMs [2]. Furthermore, the first tunneling transition is observed before one reaches zero-field on the down-sweeps of the hysteresis loops. Wernsdorfer *et al.* attribute these observations to antiferromagnetic intra-dimer magnetic interactions [27]; the magnitude of the effect suggests weak superexchange interactions via the Cl·····Cl and C–H·····Cl contacts between the two molecules within the dimer. This superexchange results in an antiferromagnetic exchange bias, whereby each half of the dimer acts as a field bias on its neighbor, resulting in a complete suppression of the zero-applied-field quantum tunneling resonance.

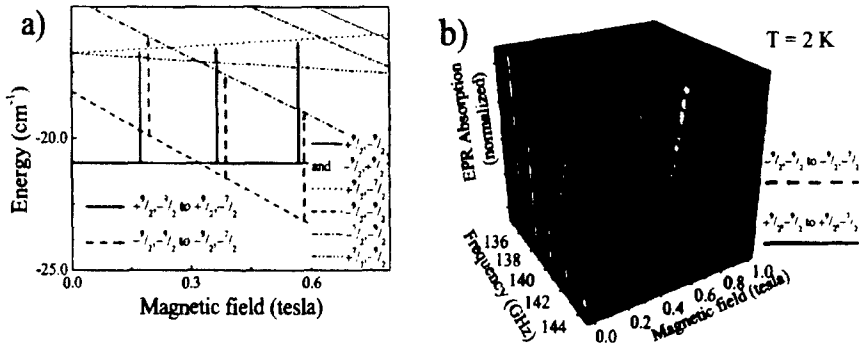

Figure 2. a) The low lying two-spin energy levels for the NA3 dimer plotted as a function of magnetic field; the most important levels have been labeled according to the scheme described in the main text. For simplicity, the calculations of these levels ignored the transverse terms in Eqs. 1 and 2. b) A 3D plot of the ground state transition(s) in NA3 obtained over a narrow field and frequency range; for clarity, the data correspond to Lorentzian fits to the original raw data. See main text for an explanation of the observed trends in the data.

In the case of two coupled SMMs, as is the case for NA3, the effective two-spin Hamiltonian is written as a sum [27]

$$\hat{H} = \hat{H}_1 + \hat{H}_2 + J\hat{S}_1 \cdot \hat{S}_2, \qquad (2)$$

where $\hat{H}_1$ and $\hat{H}_2$ are given by Eq. 1; the cross term describes the superexchange coupling between the two molecules within the dimer, and J characterizes the strength of this coupling. This adds considerable complexity to the energy level diagram, resulting in $(2S + 1) \times (2S + 1)$ levels. For NA3, the antiferromagnetic coupling (positive J) results in a zero-field ground state comprised of the degenerate ($^9/_2$,$-^9/_2$) and ($-^9/_2$, $^9/_2$) levels, as shown in Figure 2a. However, application of a field ($//z$) exceeding the exchange bias (~0.3 tesla) results in a crossing of the degenerate ($-^9/_2$,$^9/_2$)/($^9/_2$,$-^9/_2$) levels, and the ($-^9/_2$,$-^9/_2$) level, thereby changing the ground state to the latter (see Figure 2a).

In terms of the EPR, the exchange coupling results in two distinct single-spin transitions from each two-spin state, *i.e.* (M_{S1}, M_{S2}) to (M_{S1} + 1, M_{S2}) or (M_{S1}, M_{S2}) to (M_{S1}, M_{S2} + 1). However, more importantly, because of the exchange bias, the single-spin transitions now depend on the state of the other spin within the dimer. Thus, the first transitions from the two ground states, ($^9/_2$,$-^9/_2$) to ($^9/_2$,$-^7/_2$) and ($-^9/_2$,$-^9/_2$) to ($-^9/_2$,$-^7/_2$), have slightly different energies even though they both correspond to the same $-^9/_2$ to $-^7/_2$ single-spin transition. This situation is illustrated in Figure 2a. It is also now possible to excite multi-spin EPR transitions within this coupling scheme [28], though this should represent a much weaker (higher order) process. Single crystal EPR measurements enable us to test the above hypotheses.

The easy axis spectra obtained for NA3 show many similarities to the easy axis data obtained for other monomeric manganese SMMs (see *e.g.* ref. [5]), including monomeric Mn_4 clusters, many examples of which have very similar single spin Hamiltonian parameters (S, D, *etc.*) to the dimer [29]. Based on the simple exchange bias scheme developed by Wernsdorfer *et al.* [27], we

have been able to estimate the axial crystal field parameters $D \approx -0.500$ cm^{-1} and $B_4^0 \approx -7 \times 10^{-5}$ cm^{-1} for NA3; the details of this analysis will be published elsewhere [29].

The ability to measure at many different frequencies allows us to tune the ground state transition(s) to the field region where the ground state level crossing occurs in Figure 2a. In this field range, a pronounced splitting becomes apparent in the lowest field resonance, as shown in Figure 2b, *i.e.* the exchange bias has a significant affect on the EPR in this low field limit. The data in Figure 2b were obtained at 2 K so as to enhance the intensity of the ground state transition(s); thus no other transitions were observed at this low temperature. For clarity, the 3D plots in Figure 2b were made with Lorentzian fits to the data, rather than the raw data, because the signal-to-noise ratio varies considerably for the different frequencies employed. It is quite a remarkable experimental achievement to be able to make narrow band cavity measurements on such a small single crystal, and at 2 GHz intervals above 130 GHz. The splitting is due to the different energies of the respective ($^9/_2$,$-^9/_2$) to ($^9/_2$,$-^7/_2$) and ($-^9/_2$,$-^9/_2$) to ($-^9/_2$,$-^7/_2$) ground state transitions (see Figure 2a). This splitting is very robust, and is simply due to the exchange bias. By following the exchange-bias split resonance through the exchange bias field region (~0.3 T), it is apparent that the intensity transfers smoothly from the ($^9/_2$,$-^9/_2$) to ($^9/_2$,$-^7/_2$) transition to the ($-^9/_2$,$-^9/_2$) to ($-^9/_2$,$-^7/_2$) transition. This observation is consistent with the change in the ground state of the dimer at ~0.3 T. Furthermore, the switch in intensity occurs in the correct sense according to Eqs. 1 and 2, *i.e.* the high field peak grows with increasing field, and vice versa. The intensities become roughly equal when the split resonance is centered about 0.3 T, in agreement with the exchange bias field determined by Wernsdorfer *et al* [27]. Therefore, these data provide substantial support for the exchange bias model.

Using a simple model which neglects transverse terms in Eq. 2, we can predict the expected splitting of the ($^9/_2$,$-^9/_2$) to ($^9/_2$,$-^7/_2$) and ($-^9/_2$,$-^9/_2$) to ($-^9/_2$,$-^7/_2$) ground state transitions. Surprisingly, the splitting should be twice the exchange bias field, yet we observe a substantially reduced value of about 0.2 T. However, this difference does not in any way invalidate the exchange bias model, which is based on the properties of the ground state. It merely tells us that we need to develop a more complete picture of the EPR, which involves excited levels as well; this is a work in progress.

The final example which we present concerns a series of SMMs based on tetranuclear nickel clusters with varying ligands, *e.g.* the complexes $[Ni(hmp)(MeOH)Cl]_4$, $[Ni(hmp)(EtOH)Cl]_4$ and $[Ni(hmp)(tBuEtOH)Cl]_4$, which we call MeOH, EtOH and tBuEtOH for short [23]. Each complex has been predicted to have a spin $S = 4$ ground state, and an easy-axis type anisotropy. Recent low-temperature (< 1 K) hysteresis experiments have shown that the magnetic moments associated with each of these SMMs *do* exhibit resonant QTM [23]. However, in the first two complexes, the expected zero-field QTM resonance is shifted considerably away from B = 0; this behavior may again be attributed to an appreciable intermolecular exchange bias effect [27,28]. The existence of significant inter-SMM exchange interactions in these nickel based SMMs is not unexpected since the intermolecular Cl---Cl contact distances are rather short (~4.8 to 6 Å). Through systematic variations of the ligands, it is possible to tune these exchange effects, *e.g.* by varying the Cl---Cl contact distance from ~4.9 Å in the MeOH and EtOH complexes, to ~6 Å in the tBuEtOH complex.

Figure 3a shows raw field sweeps for each of the three complexes; in each case, the field is roughly aligned with the easy axis, the frequency is approximately 190 GHz, and the temperature is 10 K. Data obtained for the tBuEtOH complex are the easiest to interpret. A series of more-or-less evenly spaced double peaks is observed, with the intensity decreasing for successive pairs of

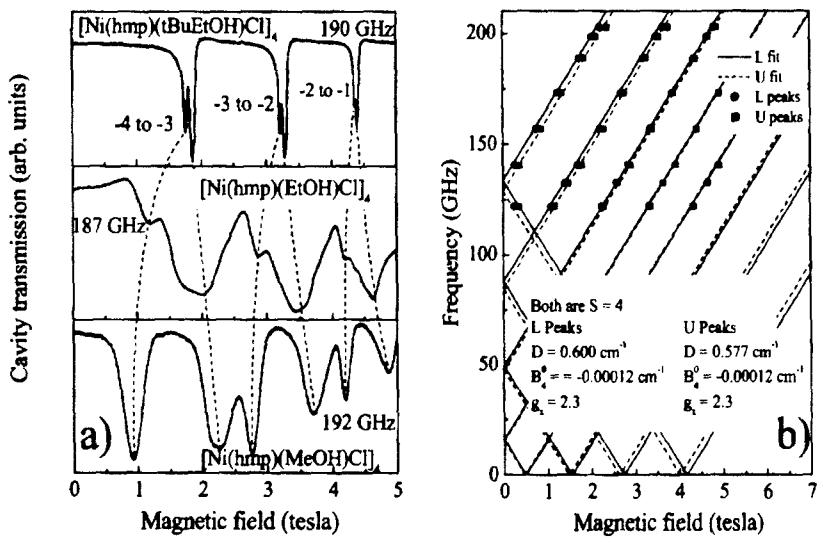

Figure 3. a) Raw EPR spectra for three different Ni_4 SMMs, obtained with the field ~parallel to the easy axes; the temperature is 10 K, and the frequencies are indicated in the figure. In the top panel, the resonances are labeled according to the M_S quantum numbers involved in the transitions. Each peak shows a splitting which increases from top to bottom; the dashed lines indicate how the peaks evolve from one complex to the next. b) Separate fits to Eq. (1) for the lower (L) and upper (U) peaks within each split doublet for the tBuEtOH complex. These fits confirm the $S = 4$ ground state and yield the diagonal components of the effective spin Hamiltonian. Similar fits (not shown) were obtained for the EtOH and MeOH complexes.

peaks. One possible interpretation of the splitting involves the existence of two species of molecule within the crystal, with slightly different crystal field parameters. Separate fits to the $S = 4$ Hamiltonian (Eq. 1) for the lower (L) and upper (U) split peaks are shown in Figure 3b. Although the fits are excellent, such an interpretation is inconsistent with X-ray studies which indicate that all molecules are crystallographically identical (with S_4 site symmetry) and that no disorder associated with the ligands exists. Careful angle dependent studies rule out crystal twinning or sample mis-alignment as a possible explanation for the splitting.

EPR spectra for the EtOH and MeOH complexes reveal considerably broader absorptions and dramatically enhanced splittings. Assignments of the peaks were determined from their temperature dependence (not shown), and from similar fits to the one shown in Figure 3b for the tBuEtOH complex. The evolution of the peaks for the three complexes is shown in Figure 3a by dashed lines, and assignments in terms of the M_S quantum numbers are given in the top panel. In every case, fits to the $S = 4$ Hamiltonian for the L and U peaks are surprisingly good (not shown), yielding the following parameters: $D_L = -0.715$ cm^{-1}, $D_U = -0.499$ cm^{-1}, $B_4^0 = -2 \times 10^{-4}$ cm^{-1} and $g_z = 2.24$ for the MeOH complex; $D_L = -0.673$ cm^{-1}, $D_U = -0.609$ cm^{-1}, $B_4^0 = -1.2 \times 10^{-4}$ cm^{-1} and $g_z = 2.20$ for the EtOH complex. Transverse terms have been

determined from powder spectra and from the same procedure as shown for Mn_{12}-acetate in Figure 1b. The dominant contribution to the ground state tunnel splitting is the quartic $B_4^4\hat{O}_4^4$ crystal field term ($B_4^4 \approx 4\times10^{-4}$ cm^{-1} for the tBuEtOH complex), which leads to a strong interaction between the $M_S = \pm4$ ground states, and to fast relaxation in zero field (ground state tunnel splitting ~12 MHz).

While an explanation for the EPR splittings in terms of crystallographically distinct Ni_4 species cannot be ruled out in the case of the EtOH and MeOH complexes (their structures are each composed of two inter-penetrating diamond lattices), it is interesting to note that the magnitudes of the splittings scale roughly with the expected strength of the exchange interactions, as determined both from the Cl---Cl contact distances and from the relative magnitudes of the exchange bias effects observed from hysteresis experiments; the MeOH complex shows an appreciably larger exchange bias effect than the EtOH complex, while the tBuEtOH complex shows no measurable exchange bias [23]. The EPR line widths and shapes are also considerably broader and more complex for the two SMMs that show a clear exchange bias effect. We note that EPR line broadening due to intermolecular exchange interactions is well documented in other SMMs [6,7], and EPR line splittings may also be expected on the basis of a simple dimer model which includes the effects of exchange between pairs of SMMs (see above). Although further investigations are needed to determine the precise origin of the splitting, it should be noted that the ability to distinguish between exchange and disorder effects will only likely be possible through single crystal measurements of the kind reported here.

SUMMARY AND CONCLUSIONS

We have described a unique cavity perturbation technique that enables high sensitivity oriented single crystal EPR measurements spanning a very wide frequency range (16 to 200+ GHz). We also present a series of brief examples of the unique capabilities of this instrumentation, with emphasis on multi-frequency oriented single crystal measurements. In particular, these studies enable precise characterizations of weak transverse interactions which turn out to be crucial as far as the quantum tunneling is concerned in SMMs.

ACKNOWLEDGEMENTS

We thank Andrew Kent and Wolfgang Wernsdorfer for stimulating discussion. Funding is provided by the National Science Foundation (DMR 0103290 and DMR0196430) and by Research Corporation.

REFERENCES

[1] J. R. Friedman, M. P. Sarachik, J. Tejada, and R. Ziolo, Phys. Rev. Lett. **76**, 3830 (1996); L. Thomas, F. Lionti, R. Ballou, D. Gatteschi, R. Sessoli, B. Barbara, Nature (London) **383**, 145 (1996).

[2] G. Christou, D. Gatteschi, D.N. Hendrickson, and R. Sessoli, MRS Bulletin, **Volume 25, No. 11**, 66 (2000).

[3] E. M. Chudnovsky, J. Tejada, *Macroscopic Quantum Tunneling of the Magnetic Moment*, (Cambridge University Press, Cambridge, 1998).

[4] Michael N. Leuenberger and Daniel Loss, Nature **410**, 789 (2001).

[5] S. Hill, S. Maccagnano, K. Park, R. M. Achey, J. M. North, and N. S. Dalal, Phys. Rev. B **65**, 224410 (2002).
[6] K. Park, M. A. Novotny, N. S. Dalal, S. Hill, and P. A. Rikvold, Phys. Rev. B **65**, 014426 (2002).
[7] Kyungwha Park, M.A. Novotny, N.S. Dalal, S. Hill, P.A. Rikvold, Phys. Rev. B **66**, 144409 (2002).
[8] S. Hill, J. A. A. J. Perenboom, N. S. Dalal, T. Hathaway, T. Stalcup, and J. S. Brooks, Phys. Rev. Lett. **80**, 2453 (1998).
[9] S. Maccagnano, R. Achey, E. Negusse, A. Lussier, M.M. Mola, S. Hill, and N.S. Dalal, Polyhedron **20**, 1441 (2001).
[10] M. Mola, S. Hill, M. Gross, and P. Goy, Rev. Sci. Instrum. **71**, 186 (2000).
[11] A. A. Mukhin, V. D. Travkin, A. K. Zvezdin, S. P. Lebedev, A. Caneschi and D. Gatteschi, Europhys. Lett., **44** (6), 778 (1998).
[12] A. Mukhin, B. Gorshunov, M. Dressel, C. Sangregorio and D. Gatteschi, Phys. Rev. B **63**, 214411 (2001).
[13] A-L. Barra, D. Gatteschi, and R. Sessoli, Phys. Rev. B **56**, 8192 (1997).
[14] A-L. Barra, D. Gatteschi, R. Sessoli, Chem-Eur. J. **6**, 1608 (2000)
[15] R. Blinc, P. Cevc, D. Arčon, N. S. Dalal and R. M. Achey, Phys. Rev. B **63**, 212401 (2001).
[16] J. F. Fernández, F. Luis, and J. Bartolomé, Phys. Rev. Lett. **80**, 5659 (1998).
[17] E. M. Chudnovsky and D. A. Garanin, Phys. Rev. Lett. **87**, 187203 (2001).
[18] D. A. Garanin and E. M. Chudnovsky, Phys. Rev. B **65**, 094423 (2002).
[19] A. Cornia, R. Sessoli, L. Sorace, D. Gatteschi, A. L. Barra, C. Daiguebonne, cond-mat/0112112 (unpublished).
[20] N. V. Prokof'ev and P. C. E. Stamp, Phys. Rev. Lett. **80**, 5794 (1998).
[21] T. Lis, Acta Cryst. B **36**, 2042 (1980).
[22] D. N. Hendrickson, G. Christou, E. A. Schmitt, E. Libby, J. S. Bashkin, S. Wang, H.-L. Tsai, J. B. Vincent, P. D. W. Boyd, J. C. Huffman, K. Folting, Q. Li, and W. E. Streib, J. Am. Chem. Soc. **114**, 2455 (1992).
[23] E-C Yang, W. Wernsdorfer, S. Hill, R. S. Edwards, M. Nakano, S. Maccagnano, L. N. Zakharov, A. L. Rheingold, G. Christou, D. N. Hendrickson, in-preparation.
[24] I. Mirebeau, M. Hennion, H. Casalta, H. Andres, H. U. Güdel, A. V. Irodova, and A. Caneschi, Phys. Rev. Lett. **83**, 628 (1999).
[25] J. R. Friedman, M. P. Sarachik, and R. Ziolo, Phys. Rev. B **58**, R14729 (1998).
[26] E. del Barco, A. D. Kent, E. Rumberger, D. Hendrickson, and G. Christou, to appear in Europhys. Lett.; cond-mat/0209167.
[27] W. Wernsdorfer, N. Aliaga-Alcalde, D. N. Hendrickson, G. Christou, Nature **416**, 406-409 (2002).
[28] W. Wernsdorfer, S. Bhaduri, R. Tiron, D.N. Hendrickson, G. Christou, Phys. Rev. Lett. **89**, 197201 (2002).
[29] R. S. Edwards, S. Hill, S. Bhaduri, N. Aliaga-Alcade, E. Bolin, S. Maccagnano, G. Christou, and D. N. Hendrickson, Polyhedron (Elsevier, in press).